Seismic structure across the rift valley of the Mid-Atlantic Ridge at 23020 ' (MARK area)' Implications for crustal accretion processes at slow spreading ridges

J Pablo Canales, John A Collins, Javier Escartin, Robert S Detrick

JOURNAL OF GEOPHYSICAL RESEARCH, VOL. 105, NO. B12, PAGES 28,411–28,425, DECEMBER 10, 2000

Seismic structure across the rift valley of the Mid-Atlantic Ridge at 23°20' (MARK area): Implications for crustal accretion processes at slow spreading ridges

J. Pablo Canales and John A. Collins

Department of Geology and Geophysics, Woods Hole Oceanographic Institution, Woods Hole, Massachusetts

Javier Escartín[1]

Instituto de Ciencias de la Tierra, Consejo Superior de Investigaciones Científicas, Barcelona, Spain

Robert S. Detrick

Department of Geology and Geophysics, Woods Hole Oceanographic Institution, Woods Hole, Massachusetts

Abstract. The results from a 53-km-long, wide-angle seismic profile across the rift valley of the Mid-Atlantic Ridge south of the Kane transform (near 23°20'N, MARK area) provide new constraints on models of tectonic extension and magmatic accretion along slow spreading mid-ocean ridges. Anomalously low middle and lower-crustal *P* wave velocities beneath the neovolcanic Snake Pit ridge are consistent with elevated axial temperatures and with the presence of 4±1% partial melt evenly distributed within the lower crust in preferentially oriented, elongated thin films. If the melt inclusions have larger aspect ratios, melt fractions can be up to 17±3%. This and other geological observations suggest that the study area is presently in a magmatically active period. The igneous crust is anomalously thin beneath both flanks of the median valley (≤2.3-2.5 km). Thus the mantle rocks observed along the western rift valley wall at Pink Hill were probably emplaced at shallow levels within the valley floor during a period of very low magma supply and were later exposed on the valley walls by normal faulting. The crust within the eastern rift valley and flanking rift mountains is seismically heterogeneous, with igneous crustal thickness variations of ≥2.2 km over horizontal distances of ~5 km. This heterogeneity indicates that the magma supply in the area has fluctuated during the last ~2 m.y. Thus magmatic and amagmatic periods at slow spreading ridges may alternate over much shorter temporal scales that previously inferred from sea surface gravity data.

1. Introduction

Seafloor-spreading processes along mid-ocean ridges depend on the thermal structure, magma supply, and tectonic processes taking place at the ridge axis. Oceanic crust formed along mid-ocean ridges with high magma supply, such as the fast spreading East Pacific Rise (EPR) or hotspot-influenced slow spreading ridges like the Reykjanes Ridge, is thought to be laterally homogeneous and composed of magmatic rocks (basalt, diabase, and gabbro). This interpretation has been inferred from seafloor observations, gravity, magnetics, marine seismic studies, ophiolite studies, and laboratory measurements of both deep-ocean and ophiolite rocks [e.g., *Christensen*, 1978; *Salisbury and Christensen*, 1978; *Kempner and Gettrust*, 1982]. This has led to the commonly accepted idea that mature fast spreading crust is layered in seismic units that reflect lithological and/or porosity changes with depth [e.g., *Vera et al.*, 1990; *White et al.*, 1992; *Detrick et al.*, 1994].

Oceanic crust formed along slow spreading ridges (<50 mm/yr full rate) like the Mid-Atlantic Ridge (MAR) has a layered seismic structure similar to that of fast spreading crust [e.g., *White et al.*, 1992; *Canales et al.*, 2000]. However, geological observations indicate that the composition of slow spreading crust is instead highly heterogeneous and/or discontinuous [e.g., *Bonatti*, 1976; *Karson et al.*, 1987; *Cannat et al.*, 1995b]. This structural variability is attributed to spatial and temporal variations in magmatic and tectonic processes that take place within the axial valley [e.g., *Tucholke and Lin*, 1994]. It has been proposed [*Pockalny et al.*, 1988] that slow spreading ridges alternate between periods of reduced magma supply when tectonics becomes the major control on the structure of the ocean crust and periods of more robust magmatic activity when crustal accretion processes resemble those at fast spreading ridges. Gravity-derived crustal thickness variations at slow spreading crust along flow lines have been interpreted as an indicator of temporal variations in magma supply. *Pariso et al.* [1995] and *Tucholke et al.* [1997] suggested that such temporal variations have a periodicity of 2-5 m.y., based on inferred relative crustal thickness variations of ±2 km along flow lines.

The alternation between magmatic and tectonic periods is commonly invoked by models that explain the emplacement of lower crust and upper mantle rocks on the seafloor (e.g., see review by *Lagabrielle et al.* [1998]). One model suggests that mantle rocks are emplaced at the seafloor by a purely tectonic

[1] Now at Laboratoire de Pétrologie, Université Pierre et Marie Curie/CNRS, Paris.

Paper number 2000JB900301
0148-0227/00/2000JB900301$09.00

process in which faulting plays the major role. Extension along low-angle faults during periods of low magma supply may unroof and expose lower crust and upper mantle rocks [e.g., *Dick et al.*, 1981; *Karson*, 1990; *Mutter and Karson*, 1992; *Tucholke and Lin*, 1994]. A variation of this tectonic model suggests that within a magmatically active segment, crustal accretion may be asymmetric, resulting in the transfer of most of the igneous crust to one side of the ridge axis and the exposure of ultramafic rocks at the conjugate side, as observed by the asymmetry of inside-outside corners [e.g., *Allerton et al.*, 2000]. An alternative model proposes a long-lived, magma-starved period during which a thin, discontinuous magmatic crust is formed by gabbroic intrusions within upper mantle peridotites [*Cannat*, 1993].

In this paper we present results from a seismic profile across the rift valley of the MAR near 23°20'N. We show that the present-day axial structure is consistent with a period of enhanced magmatism and provides important constraints on the distribution of partial melt within the axial slow spreading crust. We also show that the seismically imaged crust on the flanks of the rift valley is anomalously thin and seismically heterogeneous, providing constraints on the mechanism of emplacement of mantle rocks on the seafloor and on the periodicity of magmatic and tectonic phases of seafloor spreading at this slow spreading ridge.

2. Mid-Atlantic Ridge South of the Kane Transform

The MAR south of the Kane transform (Figure 1), known as the MARK area, is one of the best studied sections of the MAR. The present full-spreading rate at this location is ~25 mm/yr, with faster rates to the west (14 mm/yr) than to the east (11 mm/yr) during the last 3 m.y. [*Schulz et al.*, 1988]. Part of this asymmetry seems to be caused by an eastward jump of the ridge axis ~1.7 m.y. ago [*Schulz et al.*, 1988]. Off-axis geophysical studies [*Gente et al.*, 1995; *Pockalny et al.*, 1995; *Maia and Gente*, 1998] revealed a complex tectonic pattern attributed to the rapid growth and waning of short-lived segments during the last 10 m.y. The MAR between 22°30'N and 23°40'N is segmented in two spreading cells separated by a discordant zone at ~23°10'N thought to be a zero-offset discontinuity [*Karson et al.*, 1987; *Kong et al.*, 1988].

The ~40-km-long northern segment is highly asymmetrical, with a prominent elevated inside-corner massif at the western side of its intersection with the Kane transform [*Karson and Dick*, 1983] (Figure 1a). The western rift valley wall is characterized by a large fault scarp that exposes gabbro and serpentinized peridotites along the whole length of the segment [e.g., *Mével et al.*, 1991] (Figure 1b) and has been the target of several Ocean Drilling Program (ODP) legs [*Detrick et al.*, 1988; *Cannat et al.*, 1995a]. It has been interpreted to represent the initial stage of the formation of an "oceanic core complex" similar to those found in other MAR areas [*Cann et al.*, 1997; *Tucholke et al.*, 1998]. The eastern flank is characterized by smaller faults and a continuous basaltic carapace with hummocky morphology characteristic of volcanic construction [*Karson and Dick*, 1983; *Karson et al.*, 1987; *Kong et al.*, 1988; *Smith et al.*, 1995].

The ~15-km-wide rift valley floor of the northern segment is characterized by a 500- to 900-m-high, 4- to 6-km-wide, 40-km-long neovolcanic ridge (Snake Pit ridge) constructed over a highly tectonized axial valley floor [*Karson et al.*, 1987; *Karson and Brown*, 1988; *Kong et al.*, 1988; *Gente et al.*, 1991] (Figure 1). The reflective, hummocky acoustic textures that characterize the Snake Pit ridge are indicative of fresh, unsedimented basalts [*Kong et al.*, 1988], and/or of a thin sediment cover [*Gente et al.*, 1991]. Recent dating of basalts from the Snake Pit ridge using ^{238}U-^{230}Th, ^{235}U-^{231}Pa, and ^{230}Th-^{226}Ra disequilibria suggests an age of only 10±2 ka for the youngest lavas [*Sturm et al.*, 2000]. The presence of a vigorous hydrothermal system at 23°22'N [*ODP Leg 106 Scientific Party*, 1986; *Campbell et al.*, 1988] suggests elevated temperatures and heat sources at shallow or midcrustal levels.

Earlier studies of basalts collected along the neovolcanic zone showed a very homogeneous composition [*Thompson et al.*, 1986], suggesting a massive eruption from one or more, well-mixed magma chambers (consistent with compositionally diverse melts feeding the lower crust that are efficiently mixed within crustal magma chambers [*Coogan et al.*, 2000]) or successive eruptions from isolated magma chambers with a similar degree of evolution [*Karson and Brown*, 1988]. However, a more recent analysis of closely spaced basalt samples along the 40-km length of the Snake Pit ridge have revealed the existence of enriched mid-ocean ridge basalts (MORBs) near the center of the neovolcanic zone [*Donnelly et al.*, 1999], suggesting that a magma source may be located at the center of this spreading cell.

Despite the strong geological evidence suggesting that the northern segment is magmatically active, efforts to image a crustal magma body beneath this section of the ridge using near-vertical incidence seismic methods have been inconclusive [*Detrick et al.*, 1990; *Calvert*, 1995, 1997]. Wide-angle seismic data suggest that the crust along the northern segment is 4-5 km thick with no distinctive layering, indicative of a highly tectonized lithosphere during a period of low magma supply [*Purdy and Detrick*, 1986]. The axial mantle Bouguer anomalies are very irregular [*Morris and Detrick*, 1991] and differ substantially from the typical bull's-eye gravity low found along other MAR segments [*Lin et al.*, 1990; *Detrick et al.*, 1995].

3. Seismic Experiment and Data

As part of the Nobel at the Mid-Atlantic Ridge (NOMAR) Seismic Experiment (June-July 1997) [*Collins and Detrick*, 1998], we carried out an ocean bottom seismic refraction experiment at the MAR at 23°20' (profile NOMAR6). Four ocean bottom hydrophones (OBH), three ocean Reftek in a ball (ORB) hydrophones, and two ocean bottom seismometers (OBS) were deployed along a 53-km-long profile across the rift valley of the northern segment of the MARK area (Figure 1). OBS 50, and ORBs 2 and 3 were deployed in the eastern flank of the median valley; OBS 64, ORB 1, and OBH 25 on the valley floor flanking the Snake Pit ridge; and OBHs 16, 22, and 26 were deployed on the western flank of the rift valley. OBH 26 was coincident with the location of ODP Hole 920 on the flank of Pink Hill, and OBH 22 was emplaced on the summit of Pink Hill. This configuration provided a mean spacing between instruments of 4.3 km. The instrument locations are listed in Table 1.

All of the instruments recorded seismic arrivals from 329 air gun shots generated with the R/V *Maurice Ewing*'s 8420 cubic inch (138 L), 20-air-gun array towed at a depth of ~10 m. The profile was shot twice with different repetition rate: 120 s (seismic trace spacing of 252 ± 21 m), and 180 s (seismic trace spacing of 395 ± 29 m). Shot positions were obtained from the shipboard Global Positioning System (GPS) position, corrected

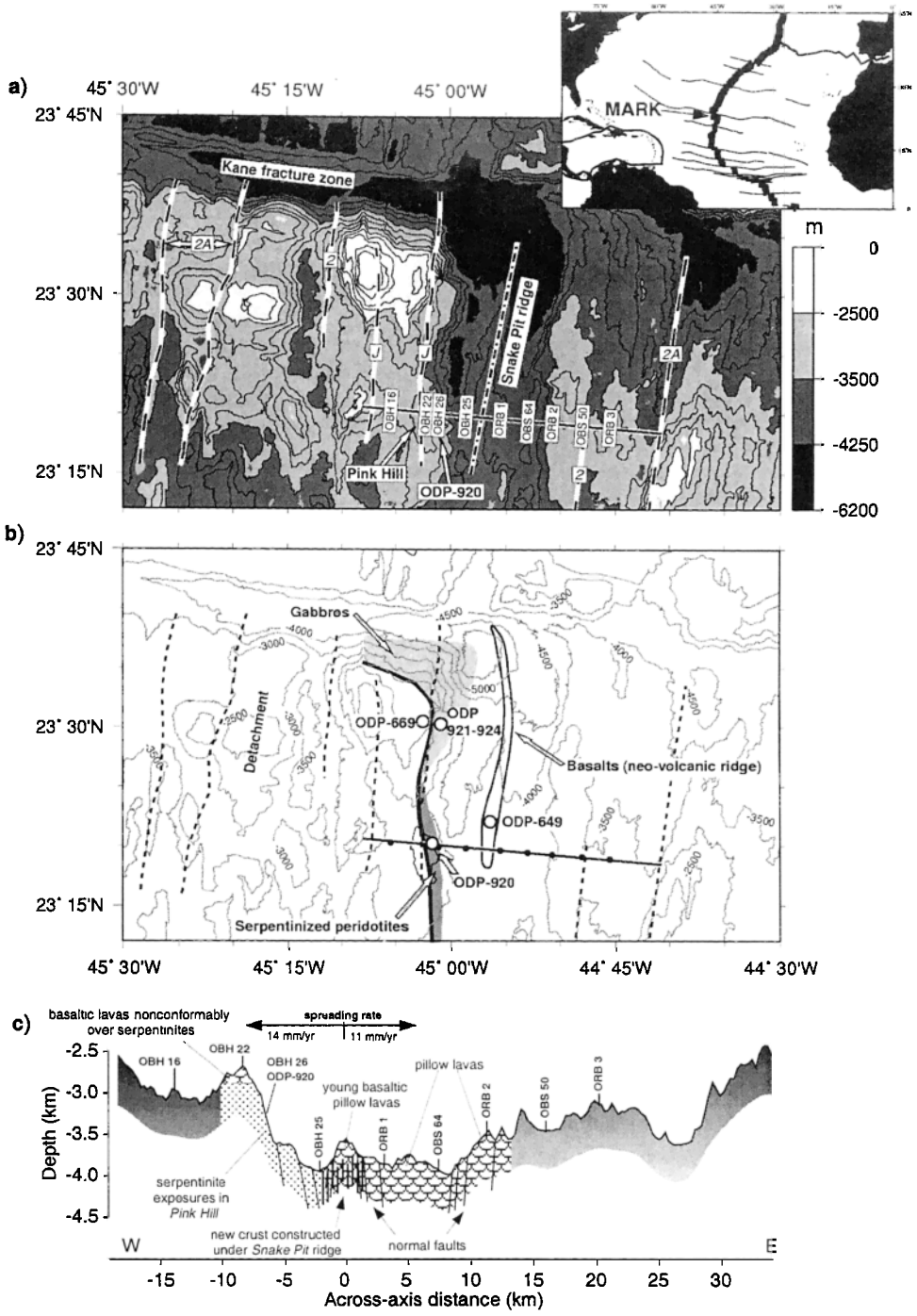

Figure 1. (a) Bathymetry map of the northern segment of the MARK area (Mid-Atlantic Ridge south of the Kane transform). Depth contours every 250 m. Thick solid line is the seismic profile NOMAR6, with instrument locations denoted by labels in boxes. The profile crosses the neovolcanic zone (Snake Pit ridge, dash-dotted line) and the location of ODP Hole 920 at Pink Hill. Dashed lines show, approximately, magnetic anomalies redrawn from *Schulz et al.* [1988], *Pockalny et al.* [1995], and *Tucholke et al.* [1998]. Inset shows the central Atlantic and the location of the MARK area. Thick line is the Mid-Atlantic Ridge, and thin lines are some major fracture zones. (b) Simplified geological map of the study area. Solid line with solid dots is profile NOMAR6. Thick solid line denotes the western wall fault along which gabbros (light shaded) and serpentinites (dark shaded) are exposed. Open circles are the location of the several ODP drill holes in the area. Other features as the neovolcanic ridge and a detachment surface at ~45°18'W [*Tucholke et al.*, 1998] are indicated. Gray depth contours every 500 m. (c) Bathymetry profile along NOMAR6. The simplified geological cross-section is modified from *Lagabrielle et al.* [1998]. Location of the instruments and ODP Hole 920 are indicated with labels. Spreading rates are from *Schulz et al.* [1988].

Table 1. Instrument Positions

Instrument	Lat., °N	Lon., °W	Depth, m	X^a, m
OBH 16	23.338	45.091	2990	-13814
OBH 22	23.333	45.038	2695	-8300
OBH 26	23.333	45.018	3316	-6330
OBH 25	23.330	44.977	3968	-2139
ORB 01	23.327	44.926	3856	3146
OBS 64	23.324	44.883	3958	7478
ORB 02	23.321	44.846	3466	11290
OBS 50	23.318	44.800	3457	16000
ORB 03	23.315	44.758	3149	20260

[a]X is the projected position of the instruments along the profile, where the coordinate origin has been arbitrarily assigned to the cross point between the profile and the summit of the Snake Pit ridge.

for the distance between the GPS antenna and the air gun array (88 m).

The seismic data were recorded by each instrument at 200 samples/s and reduced to the standard Society of Exploration Geophysicists (SEG-Y) format after correcting for the time drift of the internal clock of the instrument. For plotting and interpretation purposes, we applied a band-pass filter of 5-20 Hz to the record sections. No further data processing was required to enhance arrivals. Most of the record sections show a high signal-to-noise ratio (Figure 2), allowing a clear identification of the first-arrival travel times.

Our analysis is based on first arrivals attributed to turning rays, without making a distinction between crustal (*Pg*) and mantle (*Pn*) arrivals. We do not observe clear crust-mantle boundary reflections (*PmP*) as secondary arrivals or *Pg-PmP-Pn* triplications in the data. In contrast we observe discontinuous, high-amplitude *PmP*-like first arrivals (Figure 2) that are attributed to turning rays within a high-velocity gradient zone. We measured 2075 hand-picked travel time picks, which are shown in Figure 3 plotted against shot-receiver distance, reduced to 8 km/s and corrected for the water path travel time. For a given range, travel times can differ as much as 0.6 s, suggesting that the seismic structure varies considerably along the profile. Also, the arrivals at offsets >20 km have an apparent velocity of 8 km/s, indicating that mantle-type velocities are present at shallow levels.

We consider two sources for the travel time uncertainties. First, errors in the shot-receiver offset (±65 m, instruments were not relocated) and in the bathymetry at the ray entry point (±20 m) introduce travel time errors of ±13 ms and ±8 ms, respectively. Then we added the root-mean-sum of those errors (±15 ms, common to all the shot-receiver pairs) to the picking uncertainty that depends on the signal-to-noise ratio (SNR) of each trace. We inspected the SNR following the method of *Zelt and Forsyth* [1994]. The SNR was calculated as the square root of the ratio between the trace energy in a 250-ms window before and after the pick. The relation between the SNR and the total expected travel time uncertainty is given in Table 2. In Figure 4 we show four selected traces with their travel time pick and uncertainty representative of the four cases considered in the error estimate. Since the travel time picks were identified and selected by visually correlating adjacent traces, the uncertainty in the noisiest traces is lower than if the picks were selected in individual traces. Furthermore, the accuracy of travel time picking in noisy traces (usually related to a shot repetition rate of 120 s) was improved by comparing the seismic signature with that of traces at similar offsets with higher SNR recorded with a shot repetition rate of 180 s.

4. Results

We used the tomographic method of *Toomey et al.* [1994] to invert *P* wave travel times for both the one-dimensional (1-D) and two-dimensional (2-D) seismic structure along profile NOMAR6. The slowness (i.e., velocity) model is defined on a 56-by-10-km regular grid with a nodal spacing of 100 m in both horizontal and vertical directions. The perturbation grid had a spacing of 200 m in the vertical direction and 500 m in the horizontal direction for the 2-D inversion.

4.1. One-Dimensional Structure

We first inverted the travel time data for the best fitting depth-dependent 1-D velocity model. The motivation was to obtain a starting velocity model for the 2-D inversion that is representative of the average seismic structure of the area and to be able to interpret the 2-D structure as deviations from the regional structure. Furthermore, the 1-D inversion allows us to investigate the resolution of the model with depth and to evaluate the dependence of the results on the starting velocity model.

We tested two initial velocity models (Figure 5a): MAR23N, obtained by *Purdy and Detrick* [1986] in this same area (south of 23°15'N), and EPR9N, obtained by *Vera et al.* [1990] in 180-kyr-old crust at the EPR. The best fitting 1-D model from EPR9N is obtained after 9 iterations, and the root-mean-square (RMS) travel time residual is reduced from 214 to 101 ms. For the MAR23N, the best solution is obtained after 4 iterations, reducing the RMS from 275 ms to 97 ms. Figure 5a shows that both solutions are very similar from 1 to 4 km below the seafloor. They differ within the upper 1 km, although the mean velocities are similar (3.9 and 4.0 km/s for the solutions from EPR9N and MAR23N, respectively). This is an indication that with our data distribution the method cannot resolve the fine-scale structure within the first kilometer but only the average structure. Figure 5b shows that the resolution starts to decrease at 4 km below the seafloor (and probably is responsible for the difference in velocity between 4 and 6 km depth) and that the model cannot resolve the seismic structure for depths >6 km.

4.2. Two-Dimensional Structure

We obtained the 2-D velocity structure along profile NOMAR6 by inverting the *P* wave travel times allowing horizontal and vertical perturbations of the slowness model and using as a starting velocity model the best 1-D solution obtained from MAR23N (Figure 5a). Damping and spatial smoothing constraints need to be included in the inversion procedure to stabilize the solution. We constrained the variance of the model parameters to be 20% of the starting model. The method of *Toomey et al.* [1994] makes use of a smoothing parameter λ and a decay length τ that must be carefully chosen beforehand. We inspected several combinations of both parameters, with $\lambda_{x,y,z}$ values of 20, 40, 50, 100, and 300 and $\tau_{x,y,z}$ values of 0.5, 0.6, 0.8, 1, 1.5, and 2 km. From all of the resulting models we considered as acceptable those models that gave a normalized

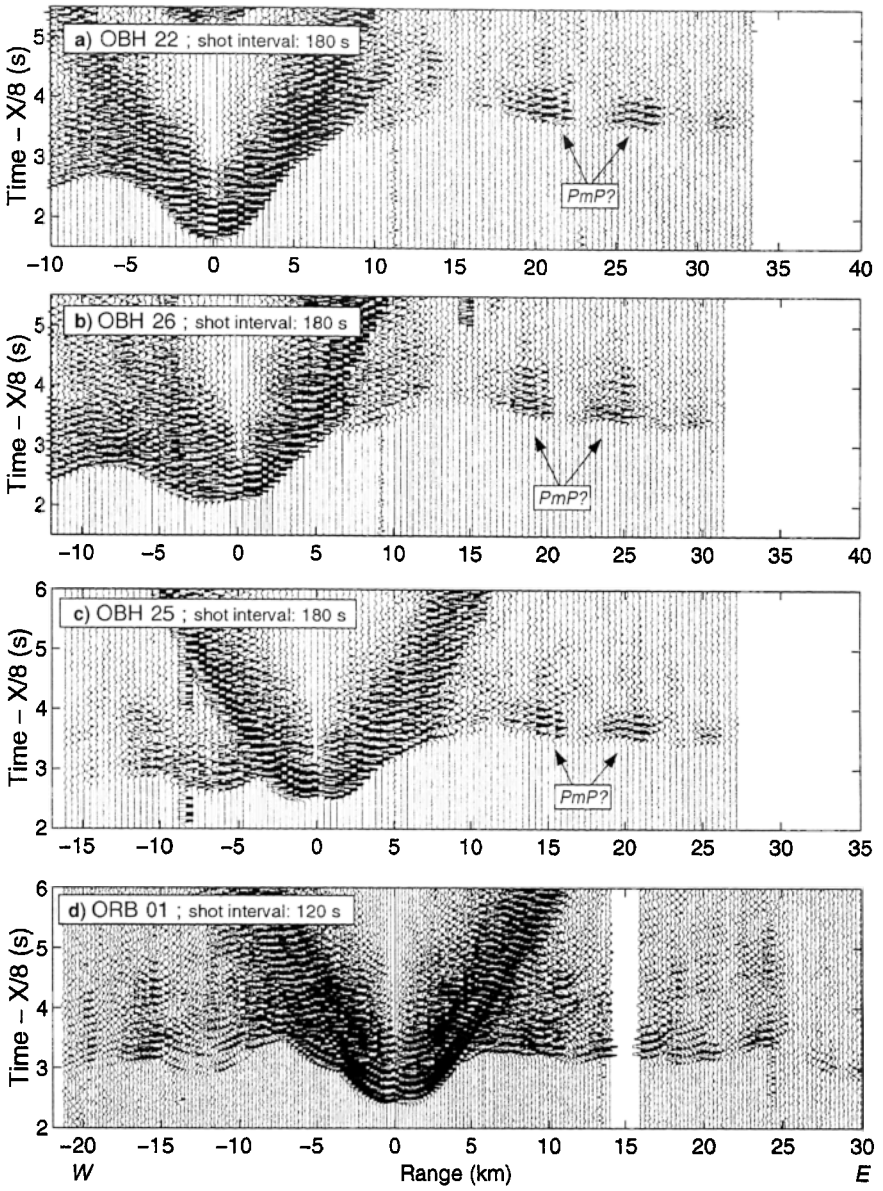

Figure 2. Observed seismic record sections from some selected instruments. Data have been reduced to 8 km/s and band-pass filtered between 5 and 20 Hz. Amplitudes have been scaled with range using a power law gain. Three cases with shot repetition rate of 180 s are shown for (a) OBH 22; (b) OBH 26; and (c) OBH 25. Note the intermittent, high-amplitude *PmP*-like arrivals. (d) One example of data recorded with shot repetition rate of 120 s (ORB 1). Note the differences in trace spacing and signal-to-noise ratio.

misfit parameter χ^2 of 1 between the predicted and observed travel times. From this subset of models we then selected our best fitting final model as the one with the larger λ (the smoothest one). Thus the final velocity model (Plate 1a) was obtained from an inversion with $\lambda_{x,\,y,\,z}$=100, $\tau_{x,\,y}$=0.6 km, and τ_z=0.5 km and gives a misfit parameter χ^2=1 with an overall RMS residual travel time of 29 ms. The comparison between the predicted and observed travel times is shown in Figure 6.

The most prominent feature of the model is the alternating pattern of mantle-type (≥7.5 km/s) and crustal-type (≤7.0 km/s) velocities between 2 and 5 km subseafloor depth across the rift valley. The eastern and western flanks of the axial valley are both characterized by mantle-type velocities at shallow levels (2-4 km below the seafloor). In contrast, the axial zone (~7 km wide centered on the Snake Pit ridge) has much lower seismic velocities. Middle and lower crustal-type velocities (~6.5 km/s) are not reached until 5-6 km below the seafloor in this area.

In Plate 1b we show the relative variation of the final velocity structure (Plate 1a) with respect to the initial 1-D velocity model obtained from MAR23N (Figure 5a). Within the uppermost kilometer of the crust, there are several positive anomalies that are spatially correlated with the footwall of several small, inward facing faults. The anomalies to the east of the Snake Pit ridge (at 8, 17.5, and 22 km model distance) have an amplitude of 0.6 km/s, while the anomaly associated with the base of Pink Hill (6 km to the west of the Snake Pit ridge) has an amplitude of 1 km/s. Also within the uppermost crust there is a prominent negative anomaly (-1.2 km/s) immediately to the west of the neovolcanic ridge.

At deeper levels the axial zone is characterized by a prominent

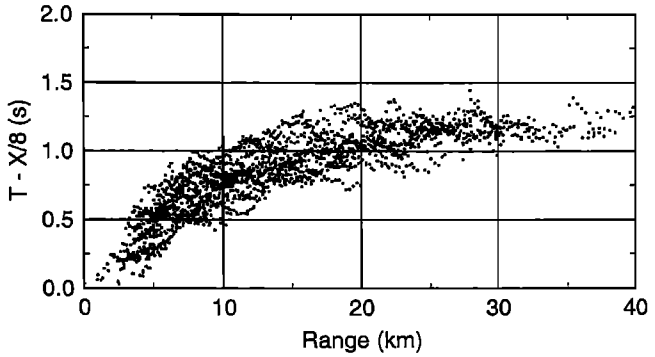

Figure 3. Observed travel times versus shot-receiver range. Times have been corrected for a reduction velocity of 8 km/s and for the travel time through the water column.

negative anomaly of -1.0 to -1.4 km/s that extends down to 5-6 km below the seafloor. At depths >1.5 km, the western rift mountains have somewhat higher seismic velocities than the eastern flank. On both sides of the axial zone there are discrete, 3- to 5-km-wide positive anomalies with amplitude of 0.6-1.2 km/s. The transition from the axial negative anomaly to the off-axis positive anomalies is sharp and occurs in a distance of 1-2 km.

In Figure 6 we show, for each instrument, the ray paths associated with the observed travel time picks, the predicted and observed travel times, and the variation of the amplitude of the seismograms with range. The amplitude-offset plots show some interesting features. For example, arrivals to the east of OBHs 22, 26, 25, and ORB 1 show strong amplitudes associated with rays that primarily sample the discrete high-velocity bodies to the east of the axial zone. This correlation suggests that the top of the high-velocity bodies may act as a discontinuous crust-mantle transition responsible for the intermittent, high-amplitude, *PmP*-like arrivals. We cannot rule out the possibility that scattered energy due to topography may also contribute to the high-amplitude arrivals.

Table 2. Total Travel Time Pick Uncertainties

SNR[a]	Number of Picks	Error, ms
SNR≥4	657	±20
2≤SNR<4	852	±30
1.5≤SNR<2	326	±40
SNR<1.5	240	±50

[a]SNR is the signal-to-noise ratio (see text for details).

4.3. Model Uncertainty and Resolution Analysis

We estimated the accuracy of our results using the Monte Carlo method [e.g., *Zhang et al.*, 1998; *Korenaga et al.*, 2000]. The uncertainty of a nonlinear inversion can be expressed in terms of the posterior model covariance matrix [e.g., *Tarantola*, 1987], which can be approximated by the standard deviation of a large number of Monte Carlo realizations assuming that all the realizations have the same probability [e.g., *Matarese*, 1993]. The uncertainty estimated by this method should be interpreted

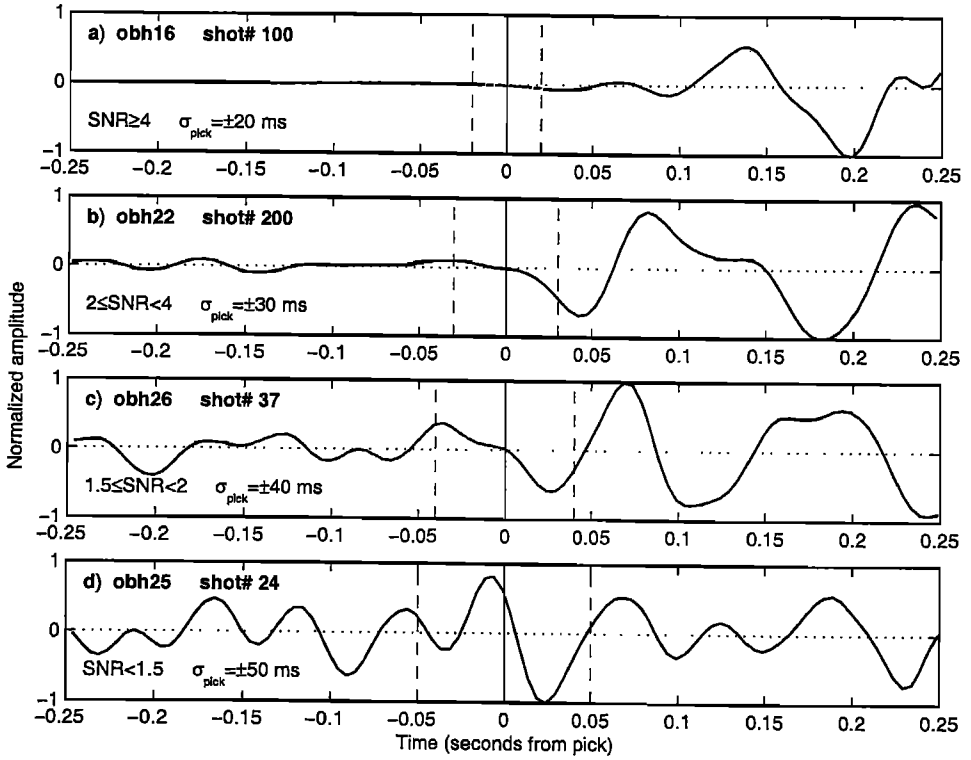

Figure 4. Selected seismic traces representative of the four cases considered for estimating the pick error based in the analysis of the signal-to-noise ratio (SNR). Horizontal axis is time, with 0 s corresponding to the pick identification (vertical solid line). The vertical dashed lines represent the total travel time uncertainties (see Table 2 and text for details). Vertical axis is trace amplitude, normalized to the maximum value observed in the window displayed. (a) Trace with SNR≥4. (b) 2≤SNR<4. (c) 1.5≤SNR<2. (d) SNR<1.5.

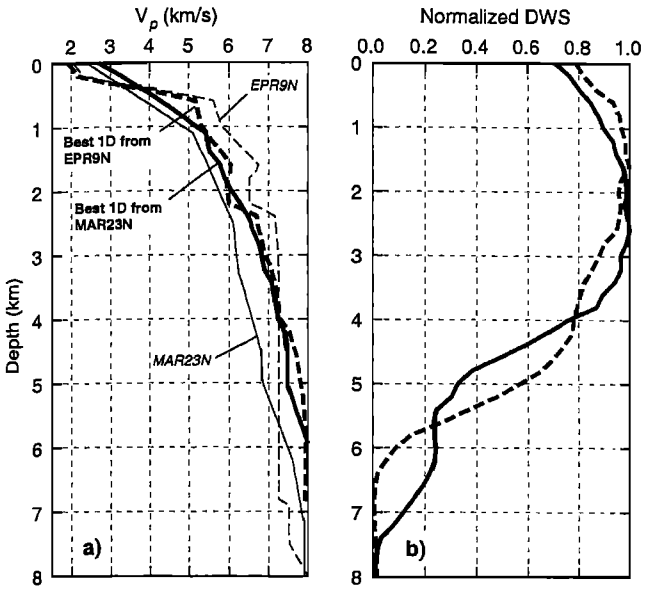

Figure 5. (a) Starting velocity models (EPR9N thin dashed line from *Vera et al.* [1990] for 180-kyr-old Pacific crust, and MAR23N thins solid line from *Purdy and Detrick* [1986] for the study area) and their best one-dimensional solution (thick dashed and solid lines, respectively). Note how different initial velocity models converge in similar results between 1 and 5 km depth. (b) Resolution in depth given by the derivative weight sum (DWS) [*Toomey et al.*, 1994].

as uncertainty for our given space model (i.e., starting velocity model and smoothing constraints). A Monte Carlo realization is computed by inverting the observed travel times (perturbed with a randomly generated noise) with a random initial velocity model. We generated 10 random initial velocity models by adding smooth perturbations randomly distributed (15 and 3 km wavelength in the horizontal and vertical direction, respectively, and maximum amplitude of ±0.4 km/s) to our best fitting model (Plate 1a). We also generated 10 random observation vectors following the method of *Zhang and Toksöz* [1998]. This method realistically simulates the travel time errors by adding to the observed travel times a common receiver random Gaussian distribution $N(0, \sigma^2_{rec})$ and a random Gaussian perturbation $N(0, \sigma^2_{\nabla t})$ to the travel time gradients. We used $\sigma^2_{rec} = 10$ ms and $\sigma^2_{\nabla t} = 15\,\mathrm{ms\,km^{-1}}$. Thus we obtained 100 Monte Carlo realizations by inverting all the combinations of the 10 initial velocity models with the 10 observation vectors, using the same model parameterization as in the final solution. With this degree of perturbation, the initial RMS misfit was ~46 ms and the χ^2 ~2.8. All of the Monte Carlo inversions converged rapidly to χ^2=1.

We show in Plate 1c that the uncertainty of the calculated velocities for most of the model is below ±0.15 km/s and locally increases to about ±0.25 km/s at the bottom of the model. Plate 1d shows the normalized DWS, a proxy to the ray density. We note that the smallest uncertainty (≤0.1 km/s) is obtained at depths shallower than ~6 km, not where the ray coverage is maximum (between 5.5 and 8 km deep). Also, the deep high-velocity areas have the largest uncertainty (≥0.2 km/s). These results are consistent with the fact that low velocities with small uncertainty predict travel times with the same accuracy as high velocities with larger uncertainties.

We conducted a series of resolution tests to assess whether our data can effectively resolve velocity anomalies of the same amplitude and dimensions as those showed in Plate 1b. We tested three major features: the 2- to 3-km-wide anomalies located within the upper kilometer (Figure 7a), the axial middle and lower crustal negative anomaly (Figure 7b), and the off-axis deep positive anomalies (Figure 7c). In each case we generated synthetic travel time data produced by synthetic anomalies (Figure 7, left) with maximum amplitude of ±20% with respect to our preferred 1-D solution (Figure 5a). This is based on the fact that the major anomalies of Plate 1b represent deviations of ±18-22% from the initial velocity model. We inverted the synthetic travel times (perturbed as in the Monte Carlo inversions) using the same model parameterization as in the final solution.

The recovered features (Figure 7, right) show that all of the major velocity anomalies can be well detected with our data and instrument distribution. The dimensions of the anomalies are well constrained, although the recovered amplitudes in all cases are somewhat lower than the initial ones. Although we showed that the recovered structure within the uppermost kilometer is strongly dependent on the starting velocity model (Figure 5a), Figure 7a shows that even small, shallow features can be well resolved with our experiment configuration if the starting velocity model is close enough to the real structure. We also tested the possibility that the deep axial negative anomaly could be an artifact produced by a negative anomaly within the middle crust smeared down in the tomography inversion. Figure 7d shows that a single ~1.5-km-thick midcrustal anomaly would be detectable by our data without affecting the deeper structure. Thus, although some percentage of the axial low-velocity zone could be an artifact produced by the off-axis high-velocity anomalies (Figure 7c), the anomalously low seismic velocities beneath the Snake Pit ridge up to 6 km below the seafloor are required by the data. We also tested that the data require the discrete high-velocity bodies imaged to the east of the Snake Pit ridge. Figure 7e shows that a single, larger structure in the eastern flank would not be imaged as two individual, smaller structures due to lateral variations in the ray coverage.

5. Interpretation and Discussion

Profile NOMAR6 can be divided in two areas with distinct seismic characteristics: the ~7-km-wide axial zone centered on the Snake Pit ridge and the areas east and west of the axial zone to which we will refer as the off-axis areas.

5.1. Off-Axis Structure

On the western ridge flank the 1 km/s positive anomaly immediately beneath OBH 26 (Plate 1b) is coincident with the belt of serpentinites exposed along the western rift valley wall [*Karson et al.*, 1987], and with ODP Hole 920 [*Cannat et al.*, 1995a]. *Miller and Christensen* [1997] calculated a mean V_p of 5.42±0.39 km/s (at a confining pressure of 200 MPa) for the ultramafic rocks representing the 200-m-long section recovered at ODP Hole 920. Although our data cannot resolve the seismic structure at this small vertical scale (200 m), the seismic velocity within the upper 1 km beneath OBH 26 increases from 3.5 to 5.5 km/s (vertical profile extracted at X=-6.3 km, Figure 8a), similar to the measurements of *Miller and Christensen* [1997]. At subseafloor depths >2.5 km, the western flank is characterized by seismic velocities >7.5 km/s (Plate 1a and Figure 8a), probably representing peridotitic mantle. Thus the igneous crust on the

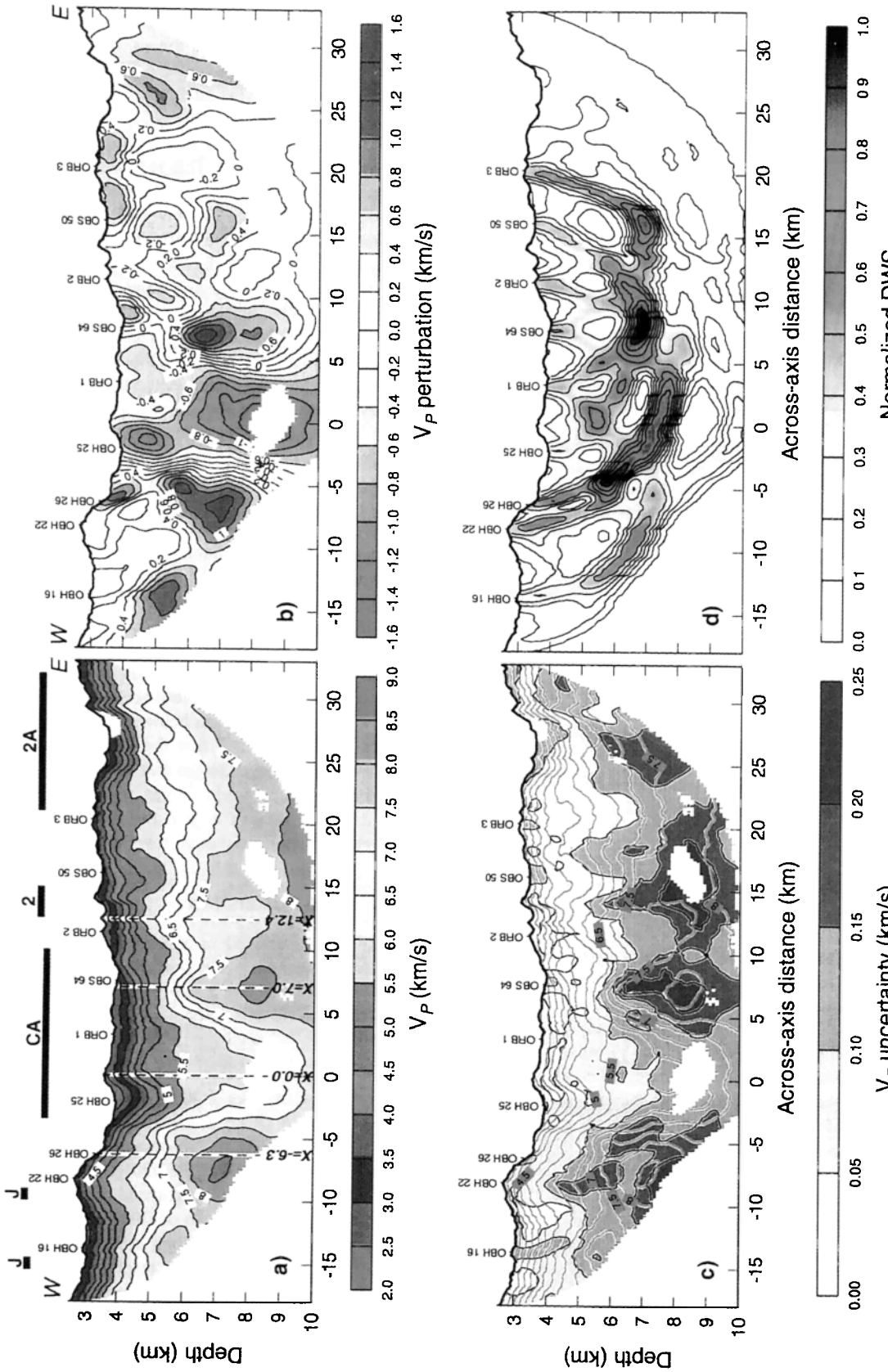

Plate 1. (a) Final two-dimensional velocity model. *P* wave velocity contours every 0.5 km/s. Thick black lines denote the width of the magnetization layers for magnetic anomalies J, 2, 2A, and central anomaly (CA) [*Schulz et al.*, 1988]. Vertical dashed lines mark the location of the velocity-depth profiles presented in Figure 8. (b) Velocity perturbation. Final model minus initial velocity model (best 1-D solution from MAR23N, Figure 5). Contours are every 0.2 km/s. (c) Uncertainty of the velocity model obtained from a Monte Carlo analysis (see text for details) Black contours are every 0.05 km/s. Red contours show the velocity model as in Plate 1a, annotated in km/s. In all of the cases we masked out the images where there is not seismic-ray coverage. (d) Ray coverage showed in terms of the normalized derivative weight sum (DWS) [*Toomey et al.*, 1994].

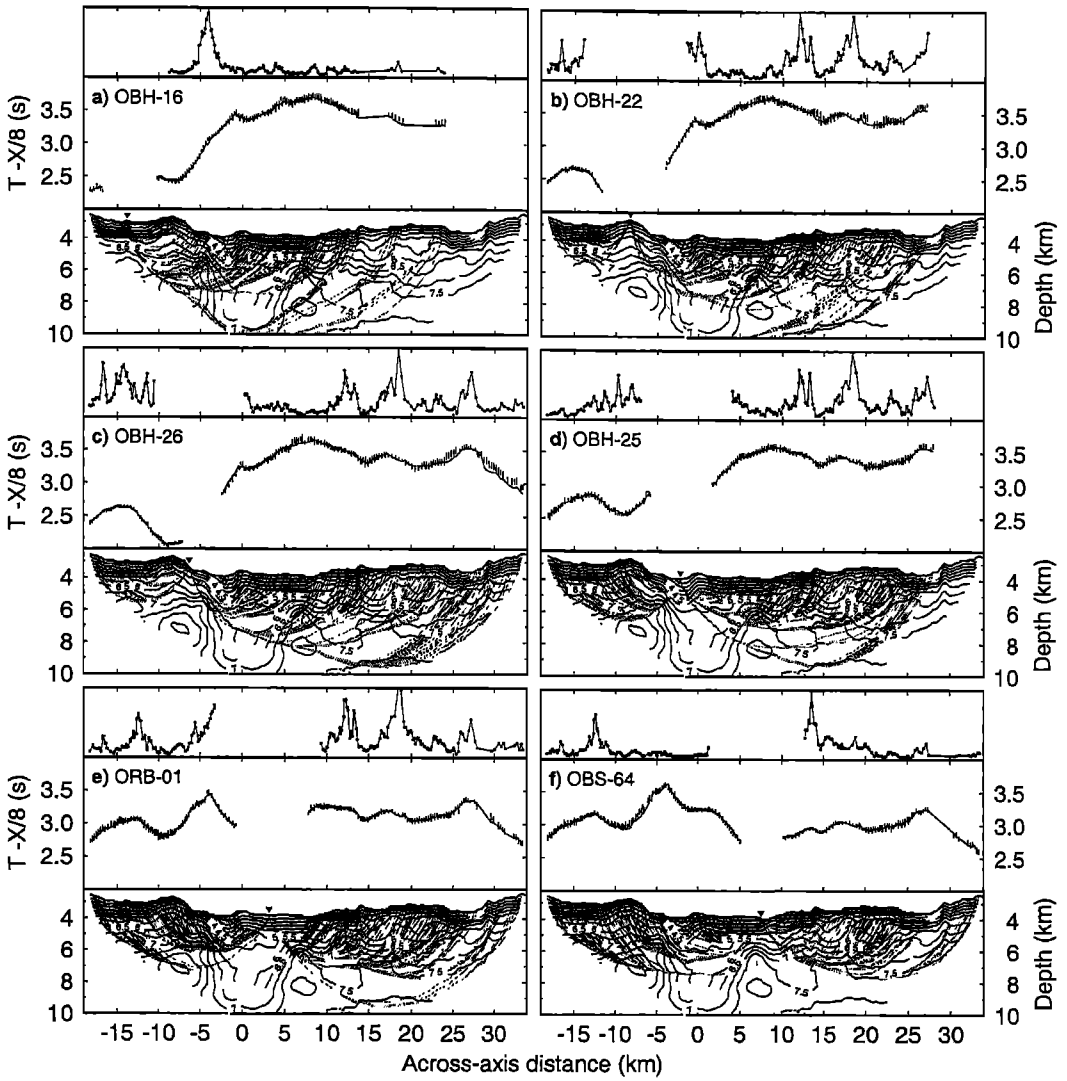

Figure 6. (a)-(i) For all the receivers from west to east. (bottom): Ray coverage for the model of Plate 1a. Annotated contours are every 0.5 km/s. Solid triangle denotes the position of the receiver. (middle): Observed (vertical bars) and predicted (solid line) travel times, reduced to 8 km/s. The height of the observed travel time bars is equal to their associated uncertainty. (top): Amplitude of the seismograms versus offset. The amplitude is measured as the maximum deflection of the seismic trace in a 0.6-s window after the first-arrival travel time pick. For each instrument the amplitudes have been amplified using a gain scale law (offset^2) and then normalized to the maximum value. The vertical axis represents one unit. Note that for OBHs 22, 26, 25, and ORB 1, rays primarily sampling the isolated high-velocity bodies to the east of the Snake Pit ridge correspond to strong increases on the amplitude of the arrivals. Compare also with the observed record sections (Figure 2).

western ridge flank is at most 2.5 km thick, and it could be thinner if velocities <7.5 km/s represent serpentinized peridotite.

Along the eastern valley flank, the positive anomalies within the uppermost crust (Plate 1b) probably reflect variations in the thickness of the extrusive layer (submersible dives and dredges reported mostly basaltic rocks to the east of the Snake Pit ridge [e.g., *Karson et al.*, 1987; *Brown and Karson*, 1988], although these observations do not extend as far east as our profile). This across-axis variation could be produced by temporal fluctuations in the volume of magma erupted on the seafloor and/or by faulting and exposure along fault scarps of basaltic rocks with lower porosity as the crust ages. We favor this later interpretation given that the anomalies are located at the foot of topographic features like small inward facing faults.

At two locations along the eastern flank (at 7 and 16 km to the east of the Snake Pit ridge, Plate 1a), we obtained velocities >7.5 km/s at very shallow depths, thus constraining the igneous crustal thickness at these locations to be <2.3 km and 3.2 km, respectively. The other areas of the eastern flank (e.g., vertical profile extracted at X=12.4 km, Figure 8a) have a seismic structure which is similar to that observed at the rift valley of other MAR segments [*Hooft et al.*, 2000] and to the average structure of young Atlantic crust [*White et al.*, 1992] (Figure 8a), with velocities increasing from 6.5 to 7.3 km/s within 2.3-4.5 km below the seafloor. These velocities are consistent with a lower crust primarily composed of gabbros or with serpentinized mantle. We find the later interpretation very unlikely since there is not a clear reason to explain why along the eastern flank some

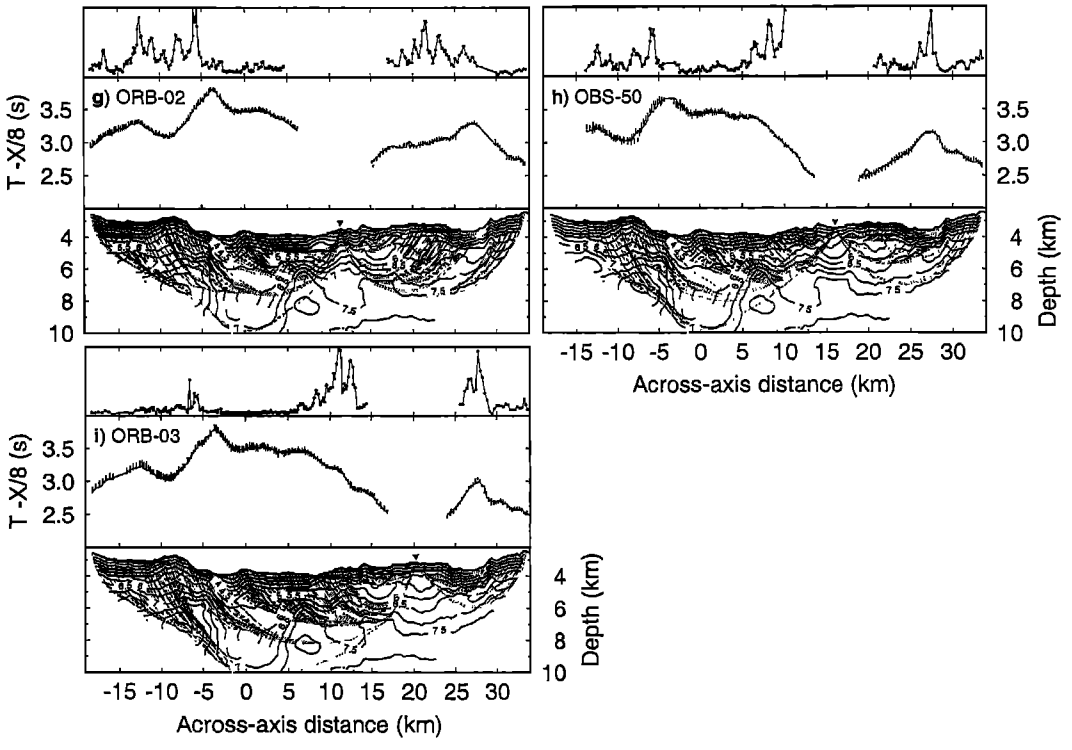

Figure 6. (continued)

sections of the mantle would be serpentinized while others would not, given the absence of large faults or tectonic features. Thus the seismic structure along the eastern flank evidences a strong lithospheric heterogeneity with igneous crustal thickness varying from ≤2.3 km to ≥4.5 km at a horizontal scale of ~5 km. This seismic pattern suggests that the magma budget in the study area has experienced rapid and important fluctuations during the last ~2 m.y.

5.2. Axial Structure

The seismic structure beneath the Snake Pit ridge is clearly anomalous. Seismic velocities to ~5 km below the seafloor are much lower than those reported by other seismic experiments in the MAR rift valley (Figure 8a) [*White et al.*, 1992; *Barclay et al.*, 1998; *Hooft et al.*, 2000; *Magde et al.*, 2000]. The uppermost crust is characterized by a negative anomaly (-1.2 km/s) immediately to the west of the Snake Pit ridge. This anomaly can be explained by a large accumulation of high-porosity lavas [e.g., *Wilkens et al.*, 1991] and/or slope debris at the base of the fault scarp. Submersible dives have reported pillow flows extending ~4 km to the west of the summit of the Snake Pit ridge (near 23°22'N) [e.g., *Brown and Karson*, 1988; *Gente et al.*, 1991]. These flows end on a 4200- to 4400-m-deep small basin at the footwall of a major fault, where OBH 25 is located (Figure 1). It is likely that the fault acts as a barrier and the lava ponds against the fault. The mixture of lava flows and talus deposits can locally increase the bulk porosity of the uppermost crust. Other factors such as fractures, hydrothermal circulation, and/or elevated temperatures within the upper 1.5 km may contribute to the negative velocity anomaly, but their relative importance is difficult to evaluate with our data.

From 2 to 5.5 km depth, the axial seismic velocities increase from 5.5 to 6.5 km/s. These velocities are consistent with serpentinized peridotite [e.g., *Miller and Christensen*, 1997] or with a gabbroic lower crust with reduced velocities due to cracks, elevated temperatures, and/or partial melt. Several factors make the first alternative unlikely. Numerous normal faults and cracks within the median valley could allow the penetration of fluids up to 6 km below the seafloor [e.g., *Toomey et al.*, 1988], altering the axial mantle. However, since the seismic structure off-axis at similar depths is that of unaltered mantle, this hypothesis seems unlikely. Alternatively, a single major fault could act as the path for fluids reaching such depths. The fault along the western valley wall is the most likely candidate, but it would have to extend across the rift valley up to 5 km to the east of the Snake Pit ridge to explain the extent of the axial low-velocity zone. Two observations make this hypothesis also unlikely. First, the seismic velocities suggest that the serpentinization front does not penetrate below 2.5 km beneath the western valley wall. Second, the fluid compositions and temperatures of the Snake Pit hydrothermal vent field suggest a maximum depth of the reaction zone of 2 km below the seafloor [*Campbell et al.*, 1988]. Furthermore, it is unlikely that the fluid pressure exceeds the lithostatic pressure at 6 km below the seafloor, as would be required to serpentinize the axial mantle by fluid penetration along opened and connected fractures at such depths.

Lithostatic pressure and ductile flow are likely to close pores and small cracks at depths >2 km. Thus the low seismic velocities within the lower crust beneath the Snake Pit ridge are most likely produced by elevated temperatures and the presence of partial melt. In order to estimate the fraction of partial melt required to explain those velocities, we compare the axial velocity structure (vertical profile extracted at X=0 km, Figure 8a) with the off-axis structure that resembles that of normal young Atlantic crust (vertical profile extracted at X=12.4 km). Thus we are assuming that the seismic structure of the axial zone will resemble that observed at ~12 km east of the Snake Pit ridge once the crust ages and cools, and the melt is extracted. An

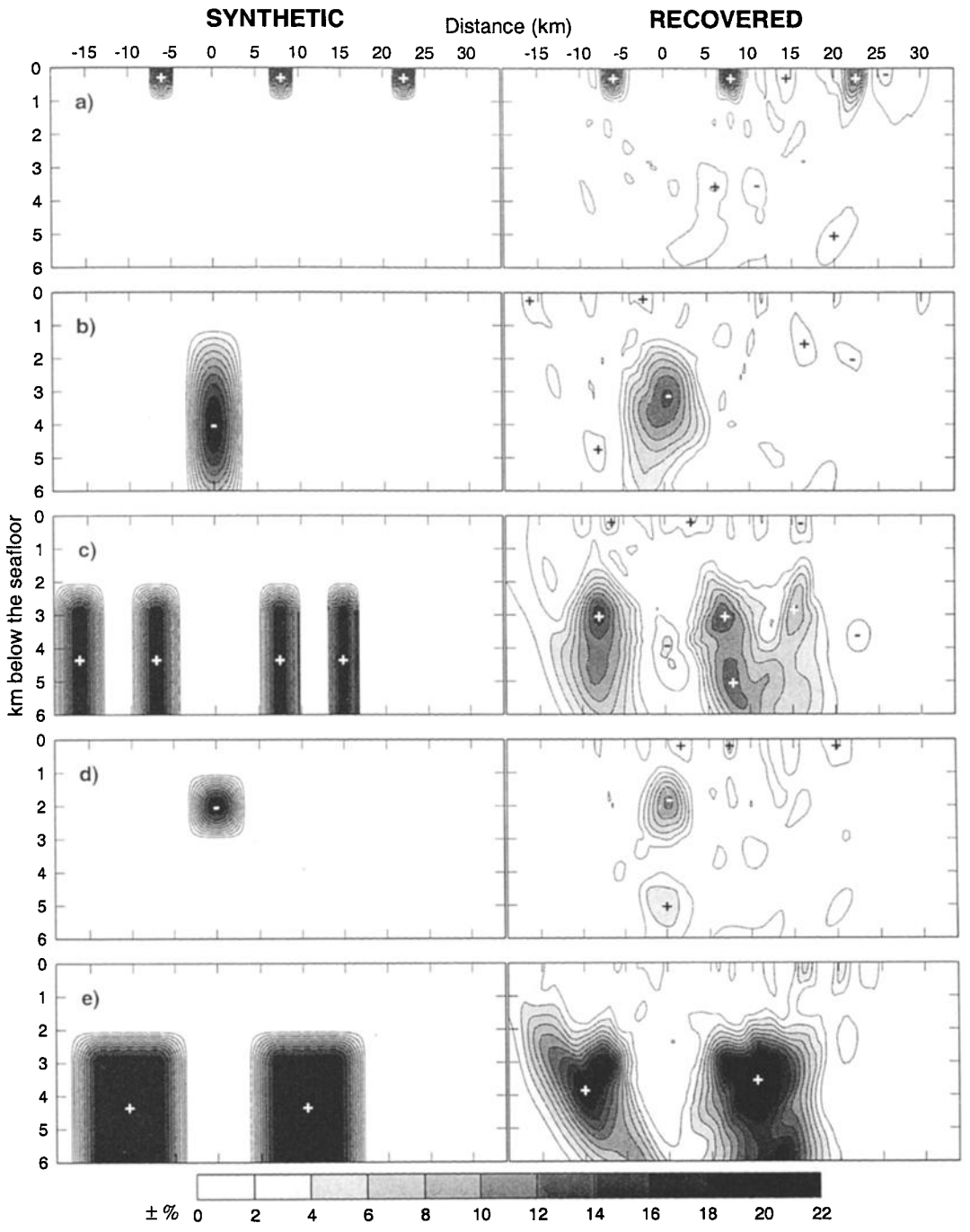

Figure 7. Resolution tests. (left): Synthetic velocity anomalies and (right) the recovered features. Contours are every ±2% of velocity perturbation. (a) Positive anomalies within the uppermost kilometer. (b) Deep axial low-velocity zone. (c) Discrete off-axis high-velocity bodies. (d) Midcrustal axial low-velocity zone. (d) Large off-axis high-velocity bodies. See text for details.

alternative hypothesis is that the axial zone is upper mantle with reduced velocities due to temperature and melt. In such a case, the seismic structure once the crust ages would resemble that observed at X=7 km or X=-6.3 km (Figure 8a). We do not explore this hypothesis since it seems inconsistent that the large melt fraction that would be required to explain the large velocity differences between X=0 km and X=-6.3 km would produce such a thin igneous crust (≤2.5 km).

We first calculate the fraction of the velocity difference between X=0 km and X=12.4 km that can be explained by elevated temperatures, and then we interpret the thermal-corrected velocity anomaly in terms of partial melt. As a thermal reference model we use the near-axis thermal structure obtained by *Henstock et al.* [1993, Figure 7g] for a slow spreading rate. We assume an anharmonic dependence of V_P with temperature (T) in the form of $\partial V_P/\partial T = -0.57\times10^{-3}$ km s^{-1} K^{-1}, as calculated for MAR gabbros by *Christensen* [1979]. We also assume that the axial temperatures cannot exceed the liquidus temperature T_L(°C) = 19.1 MgO (wt %) + 1054 [*Sinton and Detrick*, 1992]. Thus T_l=1226°C, for a mean MgO of 9 wt % measured in basalt

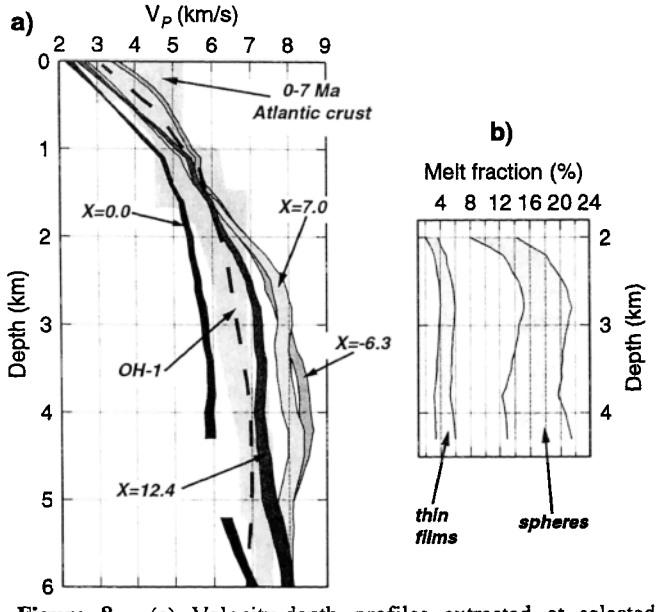

Figure 8. (a) Velocity-depth profiles extracted at selected locations along the 2-D velocity model (see Plate 1a). The width of each profile represents two standard deviations after averaging the 2-D structure extracted at the indicated positions in 2-km-wide bins and considering the uncertainties showed in Plate 1c. Dashed line corresponds to the on-axis structure at the center of segment OH-1 (MAR south of the Oceanographer transform, ~35°N), after *Hooft et al.* [2000]. Light shaded background bounds the average seismic structure of young Atlantic crust [*White et al.*, 1992]. (b) Estimated melt fraction in depth for two end-member cases: melt inclusions in elongated, thin films, and spheres. The melt fraction is interpreted to account for the differences at depths ≥2 km between the velocity-depth profile at X=0 km and at X=12.4 km, after considering thermal effects (see text for details). The width of the profiles represents error estimates obtained from the velocity uncertainties.

glasses from the Snake Pit ridge [*Bryan et al.*, 1994]. With these considerations we find that elevated temperatures above the reference model can explain 20-30% of the difference between the axial and the off-axis seismic structure at depths >2 km. This fraction should be considered as a minimum estimate, since we have not included in our calculations anelastic effects that would increase the temperature derivative of the seismic velocity [e.g., *Karato and Spetzler*, 1990; *Karato*, 1993]. Thus the following melt fraction calculations are maximum estimates.

The remaining 70-80% of the velocity anomaly can be explained in terms of partial melt once we consider the effect of the shape of the melt pockets and their orientation. We use the relationship between melt fraction and the seismic velocity measured in the direction normal to the foliation plane (since our seismic profile runs subparallel to the spreading direction) for a gabbro modal composition as reported by *Mainprice* [1997, Figure 8A]. This calculation assumes a preferred orientation of the melt inclusions. For randomly oriented inclusions the melt fraction estimates would be larger. Figure 8b shows the variation of melt fraction with depth at the axial zone for two end-member cases: thin films (aspect ratio 0.01) and spheres (aspect ratio 1). If the melt is distributed in thin films, 4±1% partial melt within the axial lithosphere is required to explain the low seismic velocities. If the melt inclusions have larger aspect ratios, the fraction of melt required reaches 17±3%. The errors in the melt fraction estimates reflect the V_p uncertainty. Laboratory studies have observed melt inclusions in ultramafic rocks with aspect ratios <0.1 [e.g., *Faul et al.*, 1994]. Thus the melt content beneath the Snake Pit ridge is likely only a few percent, with the caveat that we are assuming melt inclusions in mafic rocks, not ultramafic. Studies at the EPR reported that melt might be accumulated at midcrustal and Moho levels [*Crawford et al.*, 1999; *Dunn et al.*, 2000]. In contrast, our results suggest that in the study area the melt appears to be evenly distributed within the lower crust, although we cannot rule out the possibility that melt locally accumulates in EPR-like magma sills a few tens of meters thick [*Hussenoeder et al.*, 1996].

5.3. Implications for Magmatic and Tectonic Extension at Slow Spreading Ridges

Our results provide important constraints on models for the tectonic extension and emplacement of ultramafic rocks on the seafloor and the construction of the igneous crust at slow spreading ridges. From the different models invoked to explain the presence of ultramafic rock on the seafloor [e.g., *Lagabrielle et al.*, 1998], our results support a model in which mantle rocks are exposed on the median valley floor and covered by a basaltic carapace during a period of very low magma supply. Later normal faulting would be responsible for their exposure on the valley walls [*Mével et al.*, 1991]. The observation that on both the western and the eastern flank of the rift valley the igneous crust is, at some places, very thin (≤2.5 km) seems inconsistent with the asymmetric seismic structure predicted by tectonic models that successfully explain inside-outside corner asymmetries [e.g., *Dick et al.*, 1981; *Tucholke and Lin*, 1994] and that have been previously invoked to explain gravity observations in the MARK area [*Ballu et al.*, 1998]. Although the central magnetic anomaly suggests some degree of asymmetric magmatic accretion (Plate 1a [*Schulz et al.*, 1988]) similar to that observed in other MAR segments [*Allerton et al.*, 2000], the complicated history of ridge jumps and reorganization of the neovolcanic zone during the last 3 m.y. reported by *Schulz et al.* [1988] makes it very difficult to interpret the structure across the median valley in terms of an asymmetric pattern.

Owing to the episodic nature of magmatic activity at slow spreading ridges, few seismic experiments have been able to provide constraints on the volume of melt transferred from the mantle to the crust during magmatic episodes. At the Reykjanes Ridge, *Navin et al.* [1998] found reduced lower crustal velocities (6.5-6.8 km/s) attributable to the presence of partial melt within the axial lower crust. On the basis of electromagnetic soundings, *MacGregor et al.* [1998] suggest that the melt fraction within the axial lower crust in that region could be ≥20%. Our results (assuming thin, elongated melt inclusions with preferred orientation) suggest that the unusual low seismic velocities beneath the Snake Pit ridge can be explained by a much lower melt fraction (4%) evenly distributed in depth. This result is consistent with the hypothesis that the northern MARK segment, at least near 23°20', is presently under a magmatically active episode. This hypothesis is also supported by the young age of the axial lavas (10±2 ka [*Sturm et al.*, 2000]), by the enriched MORBs collected in the area [*Donnelly et al.*, 1999], and by the active hydrothermal vents [*Campbell et al.*, 1988].

There is much evidence that seafloor spreading along the northern MARK segment has been accommodated by tectonic stretching of the lithosphere during a period of very low magma supply during the last ~1-2 m.y. [e.g., *Karson et al.*, 1987].

About 400 kyr ago, the segment experienced an increase in magma supply resulting in seafloor spreading by magmatic accretion that persists to date. Our results suggest that the transition from a magma-starved to a magma-enriched period at a slow spreading segment is a process that can take place over a very short time period of ~80 to ~160 kyr (see the abruptness of the contact between mantle-type velocities at ~5 km off-axis and the low axial velocities, Plates 1a and 1b). Furthermore, the alternating pattern of crustal- and mantle-type velocities found along the eastern ridge flank suggests that episodes of magmatic and amagmatic spreading last over much shorter periods (~400 to ~800 kyr) than previously estimated from sea-surface gravity measurements [*Pariso et al.*, 1995; *Tucholke et al.*, 1997].

The construction of the oceanic crust at slow spreading ridges is a three-dimensional, time-dependent process that results in the creation of a highly heterogeneous oceanic lithosphere. Our results provide useful insights into some aspects of this process but, given their two-dimensional nature, leave some fundamental questions unresolved. For example, do magmatic and amagmatic cycles alternate at the same spatial and temporal scales along an entire ridge segment, or do they take place over just limited sections of the segment? Are there along-axis variations in the mechanism of emplacement of lower crustal and upper mantle rocks on the seafloor that can be related to along-axis variations in magma supply? These and other questions can only be addressed in the future with three-dimensional imaging techniques.

6. Conclusions

The conclusions of this study are as follow:

1. Anomalously low seismic velocities between 2 and 5.5 km beneath the Snake Pit ridge are consistent with elevated axial temperatures and with the presence of as little as 4±1% partial melt evenly distributed within the lower crust in preferred-oriented, elongated thin films. This suggests that the study area is presently in a magmatically active period.

2. The igneous crustal thickness along the western flank of the median valley is ≤2.5 km, while the crust beneath the eastern flank, at some locations, is ≤2.3 km thick. The anomalously thin crust on both sides of the ridge axis is inconsistent with models of asymmetric magmatic accretion and tectonic extension along low-angle faults. In contrast, it suggests that mantle rocks in this area are emplaced at shallow levels at the valley floor and later exposed on the valley walls by normal faulting.

3. Along the eastern valley flank, the seismically imaged lithosphere is highly heterogeneous, with igneous crustal thickness variations of ≥2.2 km over horizontal scales of ~5 km. This suggests that important fluctuations in the magma budget (and thus in the alternation between magmatic and amagmatic periods) have occurred more rapidly and lasted over shorter periods than previously inferred from sea surface gravity data.

4. Upper crustal P wave velocity variations of ±1 km/s across the rift valley can be related to changes in the bulk porosity of the uppermost crust due to local accumulations of lava flows and to faulting and exposure of basaltic rocks with lower porosity as the crust ages.

Acknowledgments. We thank Captain James O'Loughlin, Science Officer Joe Stennett, and the crew of the R/V *Maurice Ewing* Leg 97-04 for their help in the data acquisition. We are grateful to the WHOI OBS group, namely, Jim Dolan, Dave DuBois, John Hallinan, Ken Peal, and Beecher Wooding for their technical support. We thank Mark Behn and Hervé Nouzé for their assistance and advice during the fieldwork. We also thank the JGR Associate Editor and JGR reviewers Sara Bazin and Rob Dunn for their helpful suggestions and constructive criticism. The GMT software package [*Wessel and Smith*, 1995] was used in the preparation of this manuscript. This work was supported by the National Science Foundation grant OCE-96-33114 to the Woods Hole Oceanographic Institution. J.P.C. was partially supported by a Ministerio de Educación y Ciencia (Spain)/Fulbright Postdoctoral Fellowship (FU96-28992999). Woods Hole Oceanographic Institution contribution 10307.

References

Allerton, S., J. Escartín, and R.C. Searle, Extremely asymmetric magmatic accretion of oceanic crust at the end of slow-spreading ridge segments, *Geology, 28*, 179-182, 2000.

Ballu, V., J. Dubois, C. Deplus, M. Diament, and S. Bonvalot, Crustal structure of the Mid-Atlantic Ridge south of the Kane fracture zone from seafloor and sea surface gravity data, *J. Geophys. Res., 103*, 2615-2631, 1998.

Barclay, A.H., D.R. Toomey, and S.C. Solomon, Seismic structure and crustal magmatism at the Mid-Atlantic Ridge, 35°N, *J. Geophys. Res., 103*, 17,827-17,844, 1998.

Bonatti, E., Serpentinite protrusions in the oceanic crust, *Earth Planet. Sci. Lett., 32*, 107-113, 1976.

Brown, J.R., and J.A. Karson, Variations in axial processes on the Mid-Atlantic Ridge: The median valley of the MARK area, *Mar. Geophys. Res., 10*, 109-138, 1988.

Bryan, W.B., S.E. Humphris, G. Thompson, and J.F Casey, Comparative volcanology of small axial eruptive centers in the MARK area, *J. Geophys. Res., 99*, 2973-2984, 1994.

Calvert, A.J., Seismic evidence for a magma chamber beneath the slow-spreading Mid-Atlantic Ridge, *Nature, 377*, 410-414, 1995.

Calvert, A.J., Backscattered coherent noise and seismic reflection imaging of the oceanic crust: An example from the rift valley of the Mid-Atlantic Ridge at 23°N, *J. Geophys. Res., 102*, 5119-5133, 1997.

Campbell, A.C., et al., Chemistry of hot springs on the Mid-Atlantic Ridge, *Nature, 335*, 514-519, 1988.

Canales, J.P., R.S. Detrick, J. Lin, J.A. Collins, and D.R. Toomey, Crustal and upper mantle seismic structure beneath the rift mountains and across a nontransform offset at the Mid-Atlantic Ridge (35°N), *J. Geophys. Res., 105*, 2699-2719, 2000.

Cann, J.R., D.K. Blackman, D.K. Smith, E. McAllister, B. Janssen, S. Mello, E. Avgerinos, A.R. Pascoe, and J. Escartín, Corrugated slip surfaces formed at ridge-transform intersections on the Mid-Atlantic Ridge, *Nature, 385*, 329-332, 1997.

Cannat, M., Emplacement of mantle rocks in the seafloor at mid-ocean ridges, *J. Geophys. Res., 98*, 4163-4172, 1993.

Cannat, M., et al., *Proceedings of the Ocean Drilling Program, Initial Reports*, vol. 153, Ocean Drill. Program, College Station, Tex., 1995a.

Cannat, M., et al., Thin crust, ultramafic exposures, and rugged faulting patterns at the Mid-Atlantic Ridge (22°-24°N), *Geology, 23*, 49-52, 1995b.

Christensen, N.I., Ophiolites, seismic velocities and oceanic crustal structure, *Tectonophysics, 47*, 131-157, 1978.

Christensen, N.I., Compressional wave velocities in rocks at high temperatures and pressures, critical thermal gradients, and crustal low-velocity zones, *J. Geophys. Res., 84*, 6849-6857, 1979.

Collins, J.A., and R.S. Detrick, Seismic structure of the Atlantis fracture zone megamullion, a serpentinized ultramafic massif, *EoS Trans. AGU, 79*(45), Fall Meet. Suppl., F800, 1998.

Coogan, L.A., P.D. Kempton, A.D. Saunders, and M.J. Norry, Melt aggregation within the crust beneath the Mid-Atlantic Ridge: Evidence from plagioclase and clinopyroxene major and trace element compositions, *Earth Planet. Sci. Lett., 176*, 245-257, 2000.

Crawford, W.C., S.C. Webb, and J. Hildebrand, Constraints on melt in the lower crust and Moho at the East Pacific Rise, 9°48'N, using seafloor compliance measurements, *J. Geophys. Res., 104*, 2923-2939, 1999.

Detrick, R.S., et al., *Proceedings of the Ocean Drilling Program, Initial Reports*, vol. 106/109, Ocean Drill. Program, College Station, Tex., 1988.

Detrick, R.S., J.C. Mutter, P. Buhl, and I.I. Kim, No evidence from multichannel reflection data for a crustal magma chamber in the MARK area on the Mid-Atlantic Ridge, *Nature*, 347, 61-64, 1990.

Detrick, R., J. Collins, R. Stephen, and S. Swift, In situ evidence for the nature of the seismic layer 2/3 boundary in oceanic crust, *Nature, 370*, 288-290, 1994.

Detrick, R.S., H.D. Needham, and V. Renard, Gravity anomalies and crustal thickness variations along the Mid-Atlantic Ridge between 33°N and 40°N, *J. Geophys. Res., 100*, 3767-3787, 1995.

Dick, H.J.B., G. Thompson, and W.B. Bryan, Low-angle faulting and steady-state emplacement of plutonic rocks at ridge-transform intersections, *EoS Trans. AGU, 62*, 406, 1981.

Donnelly, K.E., C.H. Langmuir, S.L. Goldstein, and D. Desonie, Systematic distribution of E-MORB in the MARK area, *Eos Trans. AGU, 80*(46), Fall Meet. Suppl., F1086, 1999.

Dunn, R.A., D.R. Toomey, and S. Solomon, Three-dimensional seismic structure and physical properties of the crust and shallow mantle beneath the East Pacific Rise at 9°30'N, *J. Geophys. Res., 105*, 23,463-23,478, 2000.

Faul, U.H., D.R. Toomey, and H.S. Waff, Intergranular basaltic melt is distributed in thin, elongated inclusions, *Geophys. Res. Lett., 21*, 29-32, 1994.

Gente, P., C. Mével, J.M. Auzende, J.A. Karson, and Y. Fouquet, An example of a recent accretion on the Mid-Atlantic Ridge: The Snake Pit neovolcanic ridge (MARK area, 23°22'N), *Tectonophysics, 190*, 1-29, 1991.

Gente, P., R.A. Pockalny, C. Durand, C. Deplus, M. Maia, G. Ceuleneer, C. Mével, M. Cannat, and C. Laverne, Characteristics and evolution of the segmentation of the Mid-Atlantic Ridge between 20°N and 24°N during the last 10 million years, *Earth Planet. Sci. Lett., 129*, 55-71, 1995.

Henstock, T.J., A.W. Woods, and R.S. White, The accretion of oceanic crust by episodic sill intrusion, *J. Geophys. Res., 98*, 4143-4161, 1993.

Hooft, E.E.E., R.S. Detrick, D.R. Toomey, J.A. Collins, and J. Lin, Crustal thickness and structure along three contrasting spreading segments of the Mid-Atlantic Ridge, 33.5°-35°N, *J. Geophys. Res., 105*, 8205-8226, 2000.

Hussenoeder, S.A., J.A. Collins, G.M. Kent, R.S. Detrick, and the TERA Group, Seismic analysis of the axial magma chamber reflector along the southern East Pacific Rise from conventional reflection profiling, *J. Geophys. Res., 101*, 22,087-22,105, 1996.

Karato, S., Importance of anelasticity in the interpretation of seismic tomography, *Geophys. Res. Lett., 20*, 1623-1626, 1993.

Karato, S., and H.A. Spetzler, Defect microdynamics in minerals and solid-state mechanisms of seismic wave attenuation and velocity dispersion in the mantle, *Rev. Geophys., 28*, 399-421, 1990.

Karson, J.A., Seafloor spreading on the Mid-Atlantic Ridge: Implications for the structure of ophiolites and oceanic lithosphere produced in slow-spreading environments, in *Proceedings of the Symposium "Troodos 1987"*, edited by J. Malpas et al., pp. 547-555, Geol. Surv. Dept., Nicosia, Cyprus, 1990.

Karson, J.A., and J.R. Brown, Geological setting of the Snake Pit hydrothermal site: An active vent field on the Mid-Atlantic Ridge, *Mar. Geophys. Res., 10*, 91-107, 1988.

Karson, J.A., and H.J.B. Dick, Tectonics of ridge-transform intersection at the Kane Fracture Zone, *Mar. Geophys. Res., 6*, 51-98, 1983.

Karson, J.A., et al., Along-axis variations in seafloor spreading in the MARK area, *Nature*, 328, 681-685, 1987.

Kempner, W.C., and J.F. Gettrust, Ophiolites, synthetic seismograms, and ocean crustal structure, 2, A comparison of synthetic seismograms of the Samail Ophiolite, Oman, and the ROSE refraction data from the East Pacific Rise, *J. Geophys. Res., 87*, 8463-8476, 1982.

Kong, L.S.L., R.S. Detrick, P.J. Fox, L.A. Mayer, and W.B.F. Ryan, The morphology and tectonics of the MARK area from Sea Beam and Sea MARC I observations (Mid-Atlantic Ridge 23°N), *Mar. Geophys. Res., 10*, 59-90, 1988.

Korenaga, J., W.S. Holbrook, G.M. Kent, P.B. Kelemen, R.S. Detrick, H.-C. Larsen, J.R. Hopper, and T. Dahl-Jensen, Crustal structure of the southeast Greenland margin from joint refraction and reflection seismic tomography, *J. Geophys. Res., 105*, 21,591-21,614, 2000.

Lagabrielle, Y., D. Bideau, M. Cannat, J.A. Karson, and C. Mével, Ultramafic-mafic plutonic rock suites exposed along the Mid-Atlantic ridge (10°N–30°N): Symmetrical-asymmetrical distribution and implications for seafloor spreading processes, in *Faulting and Magmatism at Mid-Ocean Ridges, Geophys. Monogr. Ser.*, vol. 106, edited by W.R. Buck et al., pp. 153-176, AGU, Washington, D. C., 1998.

Lin, J., G.M. Purdy, H. Schouten, J.-C. Sempéré, and C. Zervas, Evidence from gravity data for focused magmatic accretion along the Mid-Atlantic Ridge, *Nature, 344*, 627-632, 1990.

MacGregor, L.M., S. Constable, and M. Sinha, The RAMESSES experiment, III, Controlled-source electromagnetic sounding of the Reykjanes Ridge at 57°45'N, *Geophys. J. Int., 135*, 773-789, 1998.

Magde, L.S., A.H. Barclay, D.R. Toomey, R.S. Detrick, and J.A. Collins, Crustal magma plumbing within a segment of the Mid-Atlantic Ridge, 35°N, *Earth Planet. Sci. Lett., 175*, 55-67, 2000.

Maia, M., and P. Gente, Three-dimensional gravity and bathymetry analysis of the Mid-Atlantic Ridge between 20°N and 24°N: Flow geometry and temporal evolution of the segmentation, *J. Geophys. Res., 103*, 951-974, 1998.

Mainprice, D., Modelling the anisotropic seismic properties of partially molten rocks found at mid-ocean ridges, *Tectonophysics, 279*, 161-179, 1997.

Matarese, J.R., Nonlinear travel time tomography, Ph.D. thesis, 367 pp., Mass. Inst. of Technol., Cambridge, 1993.

Mével, C., M. Cannat, P. Gente, E. Marion, J.M. Auzende, and J.A. Karson, Emplacement of deep crustal and mantle rocks on the west median valley wall of the MARK area (MAR, 23°N), *Tectonophysics, 190*, 31-53, 1991.

Miller, D.J., and N.I. Christensen, Seismic velocities of lower crustal and upper mantle rocks from the slow spreading Mid-Atlantic Ridge, south of the Kane transform zone (MARK), *Proc. Ocean Drill. Program, Sci. Results, 153*, 437-454, 1997.

Morris, E., and R.S. Detrick, Three-dimensional analysis of gravity anomalies in the MARK area, Mid-Atlantic Ridge 23°N, *J. Geophys. Res., 96*, 4355-4366, 1991.

Mutter, J.C., and J.A. Karson, Structural processes at slow-spreading ridges, *Science, 257*, 627-634, 1992.

Navin, D.A., C. Pierce, and M.C. Sinha, The RAMESSES experiment, II, Evidence for accumulated melt beneath a slow spreading ridge from wide-angle refraction and multichannel reflection seismic profiles, *Geophys. J. Int., 135*, 746-772, 1998.

Ocean Drilling Program (ODP) Leg 106 Scientific Party, Drilling the Snake Pit hydrothermal sulfide deposit on the Mid-Atlantic Ridge, lat 23°22'N, *Geology, 14*, 1004-1007, 1986.

Pariso, J. E., J.-C. Sempéré, and C. Rommeveaux, Temporal and spatial variations in crustal accretion along the Mid-Atlantic Ridge (29°-31°31'N) over the last 10 Myr: Implications from a three-dimensional gravity study, *J. Geophys. Res., 100*, 17,781-17,794, 1995.

Pockalny, R.A., R.S. Detrick, and P.J. Fox, Morphology and tectonics of the Kane transform from Sea Beam bathymetry data, *J. Geophys. Res., 93*, 3179-3193, 1988.

Pockalny, R.A., A. Smith, and P. Gente, Spatial and temporal variability of crustal magnetization of a slow spreading ridge: Mid-Atlantic Ridge (20°-24°N), *Mar. Geophys. Res., 17*, 301-320, 1995.

Purdy, G.M., and R.S. Detrick, Crustal structure of the Mid-Atlantic ridge at 23°N from seismic refraction studies, *J. Geophys. Res., 91*, 3739-3762, 1986.

Salisbury, M.H., and N.I. Christensen, The seismic velocity structure of a traverse through the Bay of Islands ophiolite complex, Newfoundland, an exposure of oceanic crust and upper mantle, *J. Geophys. Res., 83*, 805-817, 1978.

Schulz. N.J., R.S. Detrick, and S.P. Miller, Two- and three-dimensional inversions of magnetic anomalies in the MARK area (Mid-Atlantic Ridge 23°N), *Mar. Geophys. Res., 10*, 41-57, 1988.

Sinton, J.M., and R.S. Detrick, Mid-ocean ridge magma chambers, *J. Geophys. Res., 97*, 197-216, 1992.

Smith, D.K., S.E. Humphris, and W.B. Bryan, A comparison of volcanic edifices at the Reykjanes Ridge and the Mid-Atlantic Ridge at 24°-30°N, *J. Geophys. Res., 100*, 22,485-22,498, 1995.

Sturm, M.E., S.J. Goldstein, E.M. Klein, J.A. Karson, and M.T. Murrell, Uranium-series age constraints on lavas from the axial valley of the Mid-Atlantic Ridge, MARK area, *Earth Planet. Sci. Lett., 181*, 61-70, 2000.

Tarantola, A., Inverse problem theory: methods for data fitting and model parameter estimation, 613 pp., Elsevier, New York, 1987.

Thompson, G., W.B. Bryan, and S.E. Humphris, Geochemical variations in basalts erupted in the MARK area, Mid-Atlantic Ridge 23°N, *Eos Trans. AGU, 67*, 1213.

Toomey, D.R., G.M. Purdy, and S.C. Solomon, Microearthquakes beneath the median valley of the Mid-Atlantic Ridge near 23°N: Tomography and tectonics, *J. Geophys. Res., 93*, 9093-9112, 1988.

Toomey, D.R., S.C. Solomon, and G.M. Purdy, Tomographic imaging of

the shallow crustal structure of the East Pacific Rise at 9°30'N, *J. Geophys. Res., 99*, 24,135-24,157, 1994.

Tucholke, B. E., and J. Lin, A geological model for the structure of ridge segments in slow spreading ocean crust, *J. Geophys. Res., 99*, 11,937-11,958, 1994.

Tucholke, B.E., J. Lin, M.C. Kleinrock, M.A. Tivey, T.B. Reed, J. Goff, and G.E. Jaroslow, Segmentation and crustal structure of the western Mid-Atlantic Ridge flank, 25°25'-27°10' and 0-29 m.y., *J. Geophys. Res., 102*, 10,203-10,223, 1997.

Tucholke, B.E., J. Lin, and M.C. Kleinrock, Megamullions and mullion structure defining oceanic metamorphic core complexes on the Mid-Atlantic Ridge, *J. Geophys. Res., 103*, 9857-9866, 1998.

Vera, E.E., J.C. Mutter, P. Buhl, J.A. Orcutt, A.J. Harding, M.E. Kappus, R.S Detrick, and T.M. Brocher, The structure of 0- to 0.2-m.y.-old oceanic crust at 9°N on the East Pacific Rise from expanded spread profiles, *J. Geophys. Res., 95*, 15,529-15,556, 1990.

Wessel, P., and W.H.F. Smith, New version of the generic mapping tools released, *Eos Trans. AGU, 76*, 329, 1995.

White, R.S., D. McKenzie, and R.K. O'Nions, Oceanic crustal thickness from seismic measurements and rare earth element inversions, *J. Geophys. Res., 97*, 19,683-19,715, 1992.

Wilkens, R.H., G.J. Fryer, and J. Karsten, Evolution of porosity and seismic structure of upper oceanic crust: Importance of aspect ratios, *J. Geophys. Res., 96*, 17,981-17,995, 1991.

Zelt, C.A., and D.A. Forsyth, Modeling wide-angle seismic data for crustal structure: Southeastern Grenville Province, *J. Geophys. Res., 99*, 11,687-11,704, 1994.

Zhang, J., and M.N. Toksöz, Nonlinear refraction traveltime tomography, *Geophysics, 63*, 1726-1737, 1998.

Zhang, J., U.S. ten Brink, and M.N. Toksöz, Nonlinear refraction and reflection travel time tomography, *J. Geophys. Res., 103*, 29,743-29,757, 1998.

J. P. Canales, J. A. Collins, and R. S. Detrick, Department of Geology and Geophysics, Woods Hole Oceanographic Institution, 360 Woods Hole Road, Woods Hole, MA 02543. (jpcanales@whoi.edu; jcollins@whoi.edu rdetrick@whoi.edu)

J. Escartín, Laboratoire de Pétrologie, URA 736, Université Pierre et Marie Curie/CNRS, 4 Place Jussieu, F-75252 Paris Cedex 05, France. (escartin@ccr.jussieu.fr)

(Received March 28, 2000; revised July 21, 2000;
accepted August 9, 2000.)